

Groundwater feedbacks on ice sheets and subglacial hydrology

Gabriel J. Cairns¹, Graham P. Benham², and Ian J. Hewitt¹

¹Mathematical Institute, University of Oxford, Woodstock Road, OX2 6GG, Oxford, UK

²School of Mathematics and Statistics, University College Dublin, Belfield, Dublin, Ireland

February 17, 2026

Abstract

The dynamics of many of Antarctica's glaciers are modulated by a hydrological system at the base of the ice. Sedimentary basins beneath the ice bed contribute to the water budget in this hydrological system by discharging or taking up water. However, sedimentary basins are not included in most current models of ice dynamics, and little is known about their effect. In this paper we develop an idealised model of a glacier whose sliding is coupled to a subglacial hydrological system, which includes a sedimentary basin. We find that groundwater discharge (exfiltration) and recharge (infiltration) are controlled by the shape of the ice sheet and of the sedimentary basin, and that exfiltration promotes sliding whereas infiltration hinders it. Overall, the presence of a sedimentary basin leads to thicker and slower-flowing ice in the steady state. We also find that, when the ice sheet is undergoing retreating, groundwater exfiltration can lead to a positive feedback which accelerates this retreat. Our results shed light on the potential role and importance of Antarctic sedimentary basins, and how these might be incorporated into existing models of ice and subglacial hydrology.

1 Introduction

The Antarctic ice sheet is the largest body of ice on the planet, with the potential to contribute an estimated 30 cm of sea-level rise by 2100 and up to 6.9 m by 2300 under high-emission climate scenarios (Seroussi, 2024). One of the key sources of uncertainty in this estimate is our understanding of the Antarctic subglacial hydrological system (Dow, 2022; Fricker et al., 2025). This hydrological system originates mainly from water formed by melting at the base of the ice (McCormack et al., 2022) and modulates the dynamics of many of Antarctica's ice streams by affecting how rapidly the ice slides over the bed (Engelhardt et al., 1990; Morlighem et al., 2013).

One potential important contributor to the subglacial hydrological system is the exchange of groundwater with sedimentary basins. Sedimentary basins underlie large portions of Antarctica, and host substantial volumes of groundwater (Gustafson et al., 2022; Tankersley et al., 2022; Li et al., 2022; Aitken, 2023; Li and Aitken, 2024). This groundwater is discharged into the hydrological system at the base of the ice in a process known as exfiltration (or infiltration, when water instead enters the sedimentary basin), which may contribute significantly to water budgets at the base of ice streams (Christoffersen et al., 2014). However, little is currently known about the effect of these sedimentary basins on the subglacial hydrological system and hence the sliding of the ice, and the implications for contemporary ice sheet retreat.

Due to the difficulty of directly observing subglacial processes, mathematical modelling has emerged as a valuable tool in the study of subglacial hydrology (Dow, 2022), although the majority of current subglacial hydrology models do not include exfiltration from, or infiltration into, sedimentary basins. Various approaches consider water transport through subglacial conduits, a linked cavity network containing a water film (a “cavity sheet”), or flow through porous sediments (Flowers, 2015). The most frequently used state-of-the-art models combine multiple components, for example by including both a cavity sheet and a conduit system (*e.g.* Werder et al., 2013; Sommers et al., 2018). Such multi-component hydrology models have been used

to model Antarctic subglacial hydrology for both individual glacier catchments (Dow et al., 2022; Wearing et al., 2024; Zhang et al., 2024; Hayden et al., 2025) and continent-wide settings (Ehrenfeucht et al., 2025).

While some studies also include feedback of the ice on the hydrology (Cook et al., 2020; Pelle et al., 2024), two-way coupled modelling of ice and hydrology remains infrequent with state-of-the art models due to its high computational demand and the large parameter space required (Dow, 2022). As a result, relatively idealised models are more popular as a means of gaining insight into the coupling between ice sheets and subglacial hydrology (*e.g.* Lu and Kingslake, 2023; Kazmierczak et al., 2024; Haseloff et al., 2025). Such models may, for instance, work in two rather than three spatial dimensions, or consider only one component in a subglacial hydrology model (*e.g.* a conduit or a cavity sheet).

Some previous models of sedimentary basins have estimated exfiltration and infiltration driven by sediment compaction under idealised ice sheet retreat (Gooch et al., 2016; Li et al., 2022) and for contemporary ice sheet thinning rates (Robel et al., 2023). Separately, a model of two-dimensional flow neglecting compaction has been used to estimate exfiltration and infiltration driven by variations in horizontal groundwater flux (Cairns et al., 2025). Although these studies find that exfiltration from both compaction and horizontal flux variation could contribute significantly to basal water budgets, they do not model the effect of this flux on the subglacial hydrological system and its coupling with the ice sheet.

In this paper, we therefore seek to develop a simple mathematical model for ice sheet flow in one horizontal dimension, coupled to a subglacial hydrological system, which includes exfiltration and infiltration from a sedimentary basin due to both compaction and horizontal flux variation. This enables us to investigate how groundwater contributes towards or against the sliding of the ice, and where this effect is most important. We also investigate the consequences of compaction-driven exfiltration during retreat for the hydrology and ice sheet.

We introduce the governing equations of this model in Section 2, and Section 3 describes the steady states of the model when the feedback from groundwater flow on the hydrological system (and ice sheet) is weak. In Section 4, we then investigate the effect of strong groundwater flow coupling on these steady states, finding that the presence of a sedimentary basin can lead to thicker and slower-flowing ice in the steady state. In Section 5, we consider transient solutions when the ice is retreating or advancing to a new steady state, and show in particular that compaction-driven exfiltration can accelerate ice sheet retreat. In Section 6, we conclude with a discussion of our results and possible developments of the model.

2 Model development

We consider a model with one horizontal dimension in addition to the vertical, in which the ice flows along the x -direction, as shown in Figure 1. The ice has thickness $H(x, t)$, and lies on a bed at $z = b(x, t)$, where $z = 0$ refers to sea level. The ice divide is located at $x = 0$, and we assume this point also corresponds to the onset of the subglacial hydrological system. The grounded ice flow transitions into a floating ice shelf at the grounding line $x = x_g(t)$, a point which must be determined as part of the solution.

Beneath the ice is a subglacial hydrological system. For simplicity, we model this system using the ‘effective water thickness’ $h(x, t)$, which represents the average volume of water per unit area. This essentially follows the approach of treating the subglacial hydrological system as a macroporous cavity sheet (*e.g.* Alley, 1996; Creyts and Schoof, 2009; Le Brocq et al., 2009), which achieves comparable results to more complex models over long timescales (De Fleurian, 2018). Melting of the ice supplies a flux $m(x, t)$ of water to the hydrological system.

Our model also includes a sedimentary basin, with thickness $H_{sb}(x)$. We assume that the effective water thickness $h(x, t)$ is much smaller than $H(x, t)$ and $H_{sb}(x)$, so that the top of the sedimentary basin is at approximately the same position $z = b(x, t)$ as the base of the ice sheet.

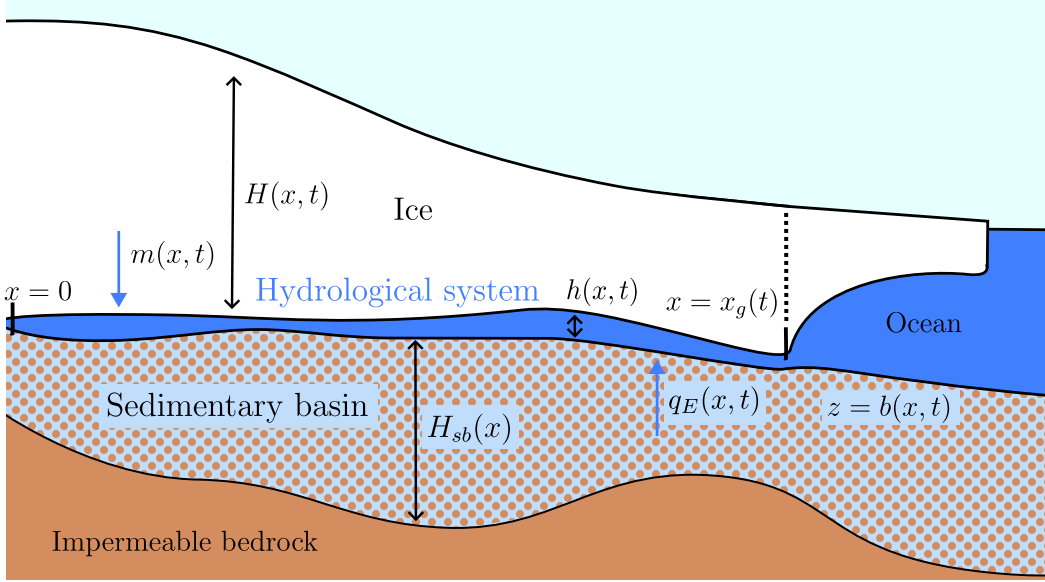


Figure 1: Schematic of the model, featuring an ice sheet with thickness $H(x, t)$ and hydrological system with effective thickness $h(x, t)$, above the bed elevation $b(x, t)$, with a sedimentary basin of thickness $H_{sb}(x)$ beneath. The grounded portion of the ice occupies $0 < x < x_g(t)$. Melting of the ice supplies a flux of water $m(x, t)$ to the hydrological system, and exfiltration (or infiltration if $q_E < 0$) from the sedimentary basin provides a flux $q_E(x, t)$.

We use q_E to denote the exfiltration (or infiltration when $q_E < 0$), the flux of water from the sedimentary basin into the hydrological system or vice versa.

2.1 Ice sheet

We adopt the ‘shallow-shelf approximation’ for ice flow, a standard model used to model relatively fast-flowing ice streams, where the ice moves primarily by sliding over the bed rather than through internal shearing (Muszynski and Birchfield, 1987; MacAyeal, 1989). This model assumes the ice has vertically-uniform velocity $u(x, t)$, so that the ice flux is given by $q(x, t) = Hu$. Conservation of mass for the ice sheet therefore gives

$$\frac{\partial H}{\partial t} + \frac{\partial}{\partial x} (Hu) = a, \quad (1)$$

where $a(x, t)$ is the net rate of ice mass accumulation by compaction of snow. For simplicity, we assume a is a known positive constant.

The ice velocity u is determined by a momentum balance, which is given by

$$\frac{\partial}{\partial x} \left(2A^{-1/n} H \left| \frac{\partial u}{\partial x} \right|^{1/n-1} \frac{\partial u}{\partial x} \right) - \tau_b(u, N) - \rho_i g H \frac{\partial}{\partial x} (H + b) = 0. \quad (2)$$

Here the first term is the divergence of the depth-integrated extensional stress in the ice. This is determined by the nonlinear rheology of ice, known as Glen’s law. The constant A is the (vertically-averaged) Glen’s law coefficient, which is well-constrained by measurements, albeit temperature-dependent. We take the corresponding exponent $n = 3$, as is commonly assumed in ice sheet models (Cuffey and Paterson, 2010).

The central term $\tau_b(u, N)$ of Equation (2) is the basal shear stress, *i.e.* the frictional force per unit area imposed on the ice by the bed. We assume this depends only on the ice velocity $u(x, t)$ and the ‘effective pressure’ $N(x, t)$ within the subglacial hydrological system. The latter is defined as the difference between the overpressure imposed by the ice and the water pressure

p_w in the subglacial water layer

$$N = \rho_i g H - p_w, \quad (3)$$

where ρ_i is the density of ice and g is gravitational acceleration. The effective pressure is zero when the water pressure is sufficient for the ice to float, and is positive when the water bears a fraction of the weight of the ice. The third term of Equation (2) is the driving stress, which corresponds to the force imposed on the ice by its own weight.

We model the basal shear stress using a ‘regularised Coulomb’ sliding law (Schoof, 2005; Gagliardini et al., 2007; Zoet and Iverson, 2020)

$$\tau_b = C_C N \left(\frac{|u|}{|u| + (C_C N / C_W)^{1/m_W}} \right)^{m_W} \operatorname{sgn}(u), \quad (4)$$

where C_W and C_C are empirical constants, and the exponent m_W is usually taken to be related to the Glen’s law exponent by $m_W = 1/n = 1/3$. The law (4) implies that the basal stress τ_b is an increasing function of N , with the limiting behaviour

$$\tau_b \sim \begin{cases} C_W |u|^{m_W} \operatorname{sgn}(u) & C_C N \gg C_W u^m, \\ C_C N \operatorname{sgn}(u) & C_C N \ll C_W u^m. \end{cases} \quad (5)$$

The use of the law (4) has been supported over a range of bed types by numerical modelling (Gagliardini et al., 2007; Joughin et al., 2019; Helanow et al., 2021) and empirical observations (Zoet and Iverson, 2020). For high effective pressures, the law (4) recovers the ‘Weertman’ sliding law frequently used in ice sheet models where hydrology has little effect on the sliding of the ice (Weertman, 1957; Fowler, 1981).

To solve the above model for $H(x, t)$, $u(x, t)$ and the free boundary $x_g(t)$, Equations (1) and (2) must be combined with spatial boundary conditions. The first of these is a prescription of no ice flux at the ice divide:

$$u = 0 \quad \text{at} \quad x = 0. \quad (6)$$

The other two boundary conditions are imposed at the grounding line. The first of these is that the ice must achieve flotation, *i.e.* the weight of the ice equals that of the displaced water

$$\rho_i g H = -\rho_w g b \quad \text{at} \quad x = x_g, \quad (7)$$

using ρ_w to denote the density of water. The second is the stress condition

$$2A^{-1/n} H \left| \frac{\partial u}{\partial x} \right|^{1/n} \frac{\partial u}{\partial x} = \frac{1}{2} \rho_i \left(1 - \frac{\rho_i}{\rho_w} \right) g H^2 \quad \text{at} \quad x = x_g. \quad (8)$$

A derivation of Equation (8), which results from considering the physics of the floating ice shelf beyond the grounding line, can be found in Schoof (2007a).

2.2 Subglacial hydrological system

The evolution of the effective water thickness $h(x, t)$ in the hydrological system is governed by an equation of mass conservation

$$\frac{\partial h}{\partial t} + \frac{\partial Q_h}{\partial x} = m + q_E. \quad (9)$$

Here Q_h is the flux of subglacial water. The source term m describes the supply of water to the hydrological system due to melting of the ice. For simplicity, we treat m as a constant parameter, whose size may be estimated by considering the melting produced by inferred geothermal heat fluxes (McCormack et al., 2022), and whose effect on the ice mass balances is included in the net accumulation a . The exfiltration q_E from the underlying sedimentary basin also appears as a source term.

For the flux Q_h , we prescribe a Darcy-like law

$$Q_h = -\frac{k}{\eta} \frac{\partial \psi}{\partial x} h, \quad (10)$$

where the hydraulic potential ψ is defined as the difference between the water pressure and hydrostatic pressure

$$\psi = p_w + \rho_w g b = \rho_i g H - N + \rho_w g b. \quad (11)$$

In Equation (10), the constant k is the effective permeability of the subglacial hydrological system and η is the viscosity of water. The former is difficult to measure and in theory depends on properties of the macroporous cavity-sheet network such as its average cavity size and connectivity. However, we can estimate a value of k based on the fact that the subglacial horizontal water flux must be large enough to evacuate the meltwater produced by geothermal heating. Haseloff et al. (2025) consider a range of values equivalent to k between 10^{-9} and 10^{-6} m², for which our estimate of 4×10^{-8} (see Table 1 in Appendix) represents an intermediate value. For simplicity, we ignore the density difference between fresh basal meltwater and saline ocean water and take all subglacial water to have the same density ρ_w .

Finally, we require a ‘closure relation’ linking h to N , which we assume can be written as a decreasing function

$$h = h(N). \quad (12)$$

This relation physically expresses how the water pressure in the cavities resists the closure of these cavities due to viscous creep of the ice. The function is decreasing because we expect cavity closure to drive water out when the water pressure p_w is low, *i.e.* when N is high. For the examples in this paper, we use the idealised relationship

$$h = \frac{E}{N}, \quad (13)$$

where E is a constant representing the ‘stiffness’ of the cavity sheet system. A particular feature of Equation (13) is that the effective water thickness $h \rightarrow \infty$ as $N \rightarrow 0$. This means that when the ice is at flotation, an unbounded amount of water can be stored beneath.

Equation (9) requires two spatial boundary conditions. As the first of these, we impose no flux of groundwater at the ice divide, where we assume the hydrological system begins,

$$Q_h = -\frac{k}{\eta} \frac{\partial \psi}{\partial x} h = 0 \quad \text{at} \quad x = 0. \quad (14)$$

For the second, we that the effective pressure is zero at the grounding line

$$N = 0 \quad \text{at} \quad x = x_g, \quad (15)$$

which is a consequence of the flotation condition (7).

2.3 Sedimentary basin

We determine the exfiltration q_E by modelling the groundwater flow in the underlying sedimentary basin. The basin is assumed to have thickness $H_{sb}(x)$, so that it occupies the region $b - H_{sb} < z < b$. We begin with the groundwater flow equation including one-dimensional vertical compaction (e.g. Lemieux et al. (2008); Li et al. (2022); Robel et al. (2023)), using $p_{sb}(x, z, t)$ to denote the water pressure in the sedimentary basin,

$$\frac{S_s}{\rho_w g} \frac{\partial p_{sb}}{\partial t} = \frac{\partial}{\partial x} \left(\frac{k_{sb}}{\eta} \frac{\partial p_{sb}}{\partial x} \right) + \frac{\partial}{\partial z} \left(\frac{k_{sb}}{\eta} \left(\frac{\partial p_{sb}}{\partial z} + \rho_w g \right) \right) + \frac{S_s \xi}{\rho_w g} \frac{\partial p_w}{\partial t}. \quad (16)$$

Here S_s is the one-dimensional specific storage, k_{sb} is the permeability of the sedimentary basin (assumed uniform and isotropic), and $0 < \xi < 1$ is the Skempton’s coefficient. The final term

depends on the water pressure $p_w = \rho_i g H - N$ in the subglacial hydrological system, which determines the overall loading stress on the sedimentary basin.

Equation (16) follows from water mass conservation, assuming the water and porous medium are weakly compressible, combined with Darcy's law for porous flow. A full derivation can be found in Lemieux (2006).

The exfiltration (or infiltration) is given by the normal Darcy flux at the top of the sedimentary basin

$$q_E = - \frac{k_{sb}}{\eta} \left(\frac{\partial p_{sb}}{\partial z} + \rho_w g - \frac{db}{dx} \frac{\partial p_{sb}}{\partial x} \right) \Big|_{z=b(x)}. \quad (17)$$

To determine this, we impose a boundary condition of no normal Darcy flux through the bottom of the sedimentary basin, where a layer of impermeable bedrock is assumed, such that

$$0 = - \frac{k_{sb}}{\eta} \left(\frac{\partial p_{sb}}{\partial z} + \rho_w g - \left(\frac{db}{dx} - \frac{dH_{sb}}{dx} \right) \frac{\partial p_{sb}}{\partial x} \right) \Big|_{z=b(x)-H_{sb}(x)}. \quad (18)$$

We may then integrate Equation (16) over the depth of sedimentary basin to obtain

$$q_E = \frac{\partial}{\partial x} \left[\frac{k_{sb}}{\eta} \int_{b-H_{sb}}^b \frac{\partial p_{sb}}{\partial x} dz \right] + \int_{b-H_{sb}}^b \left(\frac{S_s \xi}{\rho_w g} \frac{\partial p_w}{\partial t} - \frac{S_s}{\rho_w g} \frac{\partial p_{sb}}{\partial t} \right) dz, \quad (19)$$

where we have used Leibniz's integral rule.

We now make the assumption that the sedimentary basin is much longer than it is deep. This is a frequent assumption in groundwater flow problems, known as the Dupuit approximation (Bear, 2013), and is consistent with inferred Antarctic sedimentary basin geometry (Tankersley et al., 2022; Li and Aitken, 2024). This approximation implies that the water pressure is roughly hydrostatic

$$p_{sb} \approx p_w + \rho_w g(b - z). \quad (20)$$

Substituting of (20) into (19) and letting $p_w = \rho_i g H - N$ gives

$$q_E = \frac{\partial}{\partial x} \left[\frac{k_{sb}}{\eta} H_{sb} \frac{\partial}{\partial x} (\rho_i g H - N + \rho_w g b) \right] - \frac{S_s (1 - \xi)}{\rho_w g} H_{sb} \frac{\partial}{\partial t} (\rho_i g H - N). \quad (21)$$

The exfiltration in Equation (21) consists of a 'topographic' and 'compaction' term respectively. The topographic term is (minus) the divergence of the depth-integrated horizontal Darcy flux through the aquifer, which leads to exfiltration when this total flux is decreasing in the direction of flow.

The size of this term is controlled by the sedimentary basin permeability k_{sb} . Although this, like k , is difficult to measure directly in Antarctica, it can be estimated based on values from other similar sedimentary aquifers (Gooch et al., 2016; Li et al., 2022; Robel et al., 2023), estimated exfiltration fluxes (Christoffersen et al., 2014), or models of other processes such as seawater intrusion (Cairns et al., 2025).

The compaction term accounts for deformation of the porous medium, and is positive when the loading stress p_w is decreasing, due to the fact that the weakly compressible pore water expands more during unloading than the porous medium dilates. The size of this term is controlled by the specific storage S_s (and secondarily the Skempton's coefficient ξ). Like the permeability k_{sb} , this is hard to measure directly, but can be estimated based on the properties of other similar sedimentary basins and on realistic scales for q_E (Robel et al., 2023).

Other drivers of exfiltration are possible, but fall beyond our current scope. For example, basal freeze-on of subglacial water can drive exfiltration, but requires consideration of the energy balance at the ice bed (Christoffersen and Tulaczyk, 2003).

Substituting Equations (10), (12) and (21) into Equation (9) gives the combined hydrology equation

$$\frac{\partial h}{\partial t} = \frac{\partial}{\partial x} \left[\frac{kh + k_{sb}H_{sb}}{\eta} \frac{\partial}{\partial x} (\rho_i g H - N + \rho_w g b) \right] - \frac{S_s(1 - \xi)H_{sb}}{\rho_w g} \frac{\partial}{\partial t} (\rho_i g H - N) + m. \quad (22)$$

2.4 Non-dimensionalisation

We can gain insight into the model of ice and subglacial hydrology described above by non-dimensionalising the governing equations and boundary conditions. That is, for each dimensional variable, we set

$$H = [H]\hat{H}, \quad x = [x]\hat{x}, \quad \dots \quad (23)$$

where square brackets $[\cdot]$ denote the constant dimensional scales, and hats denote dimensionless variables. We then drop all hats from the notation. From here onwards, we work in dimensionless variables unless stated otherwise. However, we continue to use dimensional variables in figures and captions. The full process of non-dimensionalisation, including our choice of scales and the values used, is detailed in Appendix A.

After non-dimensionalising, Equations (1) and (2) in the ice sheet model become

$$\frac{\partial H}{\partial t} + \frac{\partial}{\partial x} (Hu) = a, \quad (24)$$

$$4\varepsilon \frac{\partial}{\partial x} \left(H \left| \frac{\partial u}{\partial x} \right|^{1/n-1} \frac{\partial u}{\partial x} \right) - \mathcal{C}N \left(\frac{|u|}{|u| + (\mathcal{C}N)^{1/m_w}} \right)^{m_w} \text{sgn}(u) - H \frac{\partial}{\partial x} (H + b) = 0. \quad (25)$$

The dimensionless parameter $\varepsilon \ll 1$ represents the size of the extensional stress term compared to the basal stress. Although this term is generally small, the extensional stresses become important near the grounding line, due to the stress balance boundary condition (8). The result is that solutions of this ice sheet model usually feature an ‘extensional stress boundary layer’, a small region near the grounding line in which the extensional stress terms become important in Equation (25), while these terms remain negligible elsewhere (Schoof, 2007a; Tsai et al., 2015). The dimensionless friction coefficient \mathcal{C} is $O(1)$, and determines how strongly the sliding of the ice is coupled to the subglacial hydrology.

In considering the exfiltration, we non-dimensionalise H_{sb} using the ice sheet thickness scale $[H]$, since sedimentary basins, like the ice sheet, are typically hundreds to thousands of metres deep (Gustafson et al., 2022; Tankersley et al., 2022). The non-dimensional version of the subglacial hydrology equation (22) is then given by

$$\lambda \frac{\partial h}{\partial t} = \frac{\partial}{\partial x} \left[(h + KH_{sb}) \frac{\partial}{\partial x} \left(H - \mathcal{E}N + \frac{b}{1 - \delta} \right) \right] + m - \Sigma H_{sb} \frac{\partial}{\partial t} (H - \mathcal{E}N). \quad (26)$$

For a given ice thickness H , Equation (26) is a nonlinear diffusion equation for N , containing several dimensionless parameters. The parameter $\delta = 1 - \rho_i/\rho_w \approx 0.1$ accounts for the density difference between water and ice, and is known. The dimensionless timescale $\lambda \ll 1$ represents the ratio of the subglacial hydrology’s natural timescale to that of the ice sheet. The fact that λ is small suggests the subglacial hydrological system generally evolves much faster than the ice sheet in the absence of compaction-driven exfiltration, but the presence of $\partial N/\partial t$ in the compaction term produces a slower evolution on a timescale $\Sigma\mathcal{E}$.

The parameter \mathcal{E} represents the characteristic size of the effective pressure relative to that of the ice overpressure, which we expect to be fairly small based on existing models of effective pressure beneath Antarctica (e.g. Ehrenfeucht et al., 2025). We take $\mathcal{E} = 0.05$, based on the the

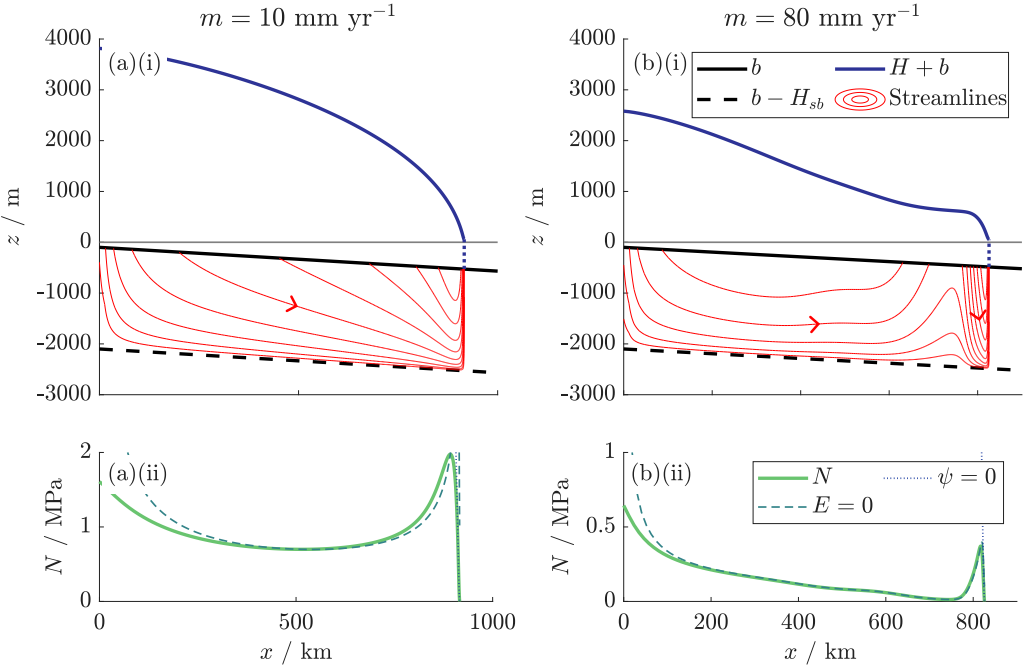


Figure 2: (i) Ice sheet profile and groundwater streamlines, and (ii) effective pressure N for (a) $m = 10 \text{ mm yr}^{-1}$ (dimensionless $m = 1$) and (b) $m = 80 \text{ mm yr}^{-1}$ (dimensionless $m = 8$), and for $K \ll 1$, with uniform sedimentary basin thickness $H_{sb} = 2000 \text{ m}$. The effective pressure is compared to the $\mathcal{E} = 0$ and $\psi = 0$ approximations given by Equation (30) and (31) respectively.

previous modelling assumption by Bueler and Brown (2009) that subglacial effective pressure is at most 5% of the overpressure.

The permeability ratio K

$$K = \frac{k_{sb}[H]}{k[h]} = \frac{1}{[m][x]} \left([H] \frac{k_{sb}\rho_i g}{\eta} \frac{[H]}{[x]} \right) \quad (27)$$

is the ratio of a typical horizontal flux through the sedimentary basin to that of the subglacial cavity sheet. The size of K determines the flux of water transported through the sedimentary basin rather than the cavity sheet, along with the overall scale of topographic exfiltration. Taking a value $k_{sb} = 1.6 \times 10^{-12} \text{ m}^2$, as is consistent with the findings of Cairns et al. (2025), gives $K = 1$ (see Appendix). Values of k_{sb} could range as low as 10^{-17} m^2 (giving $K \approx 6 \times 10^{-6}$) (e.g. Gooch et al., 2016), but are unlikely to exceed 10^{-11} m^2 (giving $K \approx 6$). Finally, the parameter

$$\Sigma = \frac{\rho_i S_s (1 - \xi) [H]^2}{\rho_w [m][t]}. \quad (28)$$

determines the relative size of exfiltration driven by compaction. Robel et al. (2023) use a range of S_s from 1×10^{-7} to 1×10^{-4} , which give Σ between 5×10^{-3} and 5. In this paper, we therefore consider values ranging from $S_s = 0 \text{ m}^{-1}$ ($\Sigma = 0$) to $S_s = 2.37 \times 10^{-4} \text{ m}^{-1}$ ($\Sigma = 12$).

Equations (24), (25) and (26) are combined with non-dimensional analogues of the boundary conditions (6), (7), (8), (14) and (15), which may be found in the Appendix.

3 Steady ice sheet with weak groundwater flow

Firstly, to gain an intuition of the model, we consider the steady states in the limit $K \ll 1$, in which the sedimentary basin does not exert any effect on the subglacial effective pressure or ice thickness, although it is still possible to plot the limiting streamlines of groundwater flow. In the steady state, the compaction terms do not play a role, since these require time dependence by definition. (We obtain figures for the ' $K \ll 1$ ' case by using the value $K = 0$, although we

refrain from referring to them as ‘ $K = 0$ ’ as this would imply no groundwater flow occurs at all.)

3.1 Ice sheet and effective pressure for weak groundwater flow

Figure 2(a)(i) and (ii) show a case where the melt rate $m = 10 \text{ mm yr}^{-1}$ (dimensionless $m = 1$) is relatively low. As a result, the sliding law (4) closely approximates to the limiting case $\tau_b \approx |u|^{m_w}$ away from the grounding line, resulting in a ‘convex’ ice sheet profile, which becomes steeper in the direction of flow.

Near the grounding line, the sliding stress $\tau_b \rightarrow 0$, due to the condition (15) that $N \rightarrow 0$ as $x \rightarrow x_g$. This results in a boundary layer near x_g , where $\tau_b \approx \mathcal{C}N$ and the extensional stress terms in (25) become significant. This boundary layer, which determines x_g , has been described by Tsai et al. (2015).

The corresponding effective pressure is shown in Figure 2(a)(ii). Integrating the steady state of Equation (26) subject to the no-flux condition (14) gives that

$$(h(N) + KH_d) \frac{\partial}{\partial x} \left(H - \mathcal{E}N + \frac{b}{1-\delta} \right) + mx = 0. \quad (29)$$

Since \mathcal{E} is relatively small, the solution for $N(x)$ follows two approximate solutions in different regions. Away from the grounding line $x = x_g$ (and from $x = 0$), the solution is roughly given by the case when $\mathcal{E} = 0$,

$$h(N) \sim mx \left[-\frac{\partial}{\partial x} \left(H + \frac{b}{1-\delta} \right) \right]^{-1} - KH_d, \quad \text{for } x_g - x \gg \mathcal{E}. \quad (30)$$

Since $h(N)$ is a decreasing function (we take $h(N) = 1/N$ in particular), Equation (30) implies that increasing m decreases N away from the grounding line. Equation (30) breaks down for small m and/or large K , as when h becomes small the large effective pressure N can no longer be neglected in the hydraulic potential.

Near the grounding line, provided that $h(N) \rightarrow \infty$ as $N \rightarrow 0$, as is the case for our choice of $h(N)$, the solution is approximately given by equating the hydraulic potential $\psi = 0$, such that

$$N \sim \frac{1}{\mathcal{E}} \left(H + \frac{b}{1-\delta} \right) \quad \text{for } x_g - x \ll \mathcal{E}. \quad (31)$$

The effective pressure in Figure 2(a)(ii) exhibits a local maximum near the grounding line as the solution transitions from Equation (30) to Equation (31). The local behaviour (31) of N near the grounding line can be thought of as a boundary layer associated with the small parameter \mathcal{E} , but should not be confused with the extensional stress boundary layer in the ice sheet associated with the small parameter ε .

Because the grounding line position of the ice sheet is determined by the extensional stress boundary layer, in which the sliding stress $\tau_b \sim \mathcal{C}N$, Equation (31) suggests that the melt rate m and sedimentary basin do not affect the steady grounding line position to leading order, although they may have a small effect via sub-leading order terms.

Figure 2(b)(i) and (ii) show the steady state of the ice and hydrology at a higher melt rate $m = 80 \text{ mm yr}^{-1}$ (dimensionless $m = 8$). Although the ice sheet in Figure 2(b)(i) follows a similar convex shape to the $m = 10 \text{ mm yr}^{-1}$ case near the ice divide $x = 0$, it assumes a much shallower shape nearer the grounding line before steepening again. As a result of this shallow portion, the ice sheet is thinner overall, reaching a maximum thickness of around 3000 m, rather than 4000 m as for $m = 10 \text{ mm yr}^{-1}$. Since the steady state ice flux from (24) is simply the integral of the accumulation a , thinner ice must also be faster-flowing.

The reason for this changed shape lies in the effective pressure N , seen in Figure 2(b)(ii). When m is increased, the overall size of N away from the grounding line is decreased, following

the $\mathcal{E} = 0$ approximate solution (30). However, the $\psi = 0$ approximate solution (31) still holds near the grounding line, meaning that the effective pressure continues to exhibit a maximum near x_g . In this case, N is sufficiently low that the basal stress given by (4) behaves as $\tau_b \sim CN$, rather than $\tau_b \sim |u|^{mw}$, over much of the interior of the ice sheet. Since the basal friction balances the driving stress in (25), the reduced basal friction results in a lower $|\partial H/\partial x|$ and hence a shallower ice profile. However, near the ice divide $x = 0$, the velocity becomes sufficiently low that the behaviour $\tau_b \approx |u|^{mw}$ takes over once again, resulting in a reversion to the convex ice sheet profile.

There is also a retreat of the grounding line in Figure 2(b)(i) compared to Figure 2(a)(i), from around 920 km to 830 km. This is due to the sub-leading order effect of m in the behaviour of N near x_g , which reduces the effective pressure and hence the basal stress in the extensional stress boundary layer of the ice.

3.2 Streamlines of groundwater flow

We now consider the groundwater flow, exfiltration and infiltration for $K \ll 1$. Equation (21), after non-dimensionalising, gives the exfiltration in the steady state as

$$q_E = K \frac{\partial}{\partial x} \left[H_{sb} \frac{\partial}{\partial x} \left(H - \mathcal{E}N + \frac{b}{1-\delta} \right) \right]. \quad (32)$$

Upon substituting in Equation (29) for the hydraulic potential gradient, we have

$$\begin{aligned} q_E &= -K \frac{\partial}{\partial x} \left[H_{sb} \frac{mx}{h + KH_{sb}} \right] \\ &= -\frac{KmH_{sb}}{h + KH_{sb}} - \frac{Kmx}{h^2(h + KH_{sb})^2} \frac{\partial}{\partial x} \left(\frac{H_{sb}}{h} \right). \end{aligned} \quad (33)$$

This implies that a necessary (but insufficient) condition for $q_E \geq 0$ (*i.e.* exfiltration) is that

$$\frac{\partial}{\partial x} \left(\frac{H_{sb}}{h(N)} \right) < 0, \quad (34)$$

that is, the ratio of the groundwater flux through the sedimentary basin to that through the cavity sheet system is decreasing. This could be achieved through the sedimentary basin thickness H_{sb} decreasing in the direction of flow, as considered previously by Cairns et al. (2025). The other possibility is that $h(N)$ is increasing, *i.e.* N is decreasing.

The streamlines of groundwater flow in the limit $K \ll 1$ with constant $H_{sb} = 2000$ m are plotted in Figure 2(a)(i) and (b)(i). In the $m = 10$ mm yr⁻¹ case (Figure 2(a)(i)), groundwater infiltrates into the sedimentary basin almost everywhere, apart from a small region of exfiltration near the grounding line. This is because the condition (34) implies for constant H_{sb} that exfiltration can only occur where $\partial N/\partial x < 0$. In the $m = 80$ mm yr⁻¹ case (Figure 2(b)(i)), however, this pattern is modified by an intermediate region of exfiltration, occurring where the flattening of the ice surface leads to decreasing N following the $\mathcal{E} = 0$ approximate solution (30). If we increased K , we would expect this exfiltration to further reinforce the lowering of N and consequent flattening of the ice.

An alternative way to think of q_E is in terms of the hydraulic potential ψ . For constant H_{sb} , q_E is proportional to $\partial^2 \psi / \partial x^2$ by Equation (32). Away from the grounding line, ψ is dominated by the ice overpressure H , so that the ‘convex’ ice profile in Figure 2(a)(i) leads to infiltration. Exfiltration only occurs near the grounding line, where the $\psi \approx 0$ approximate solution (31) leads to a change in sign of $\partial^2 \psi / \partial x^2$. In Figure 2(b)(i), however, the more complex shape of the ice means $\partial^2 \psi / \partial x^2$ temporarily changes sign away from the grounding line, leading to an additional region of exfiltration.

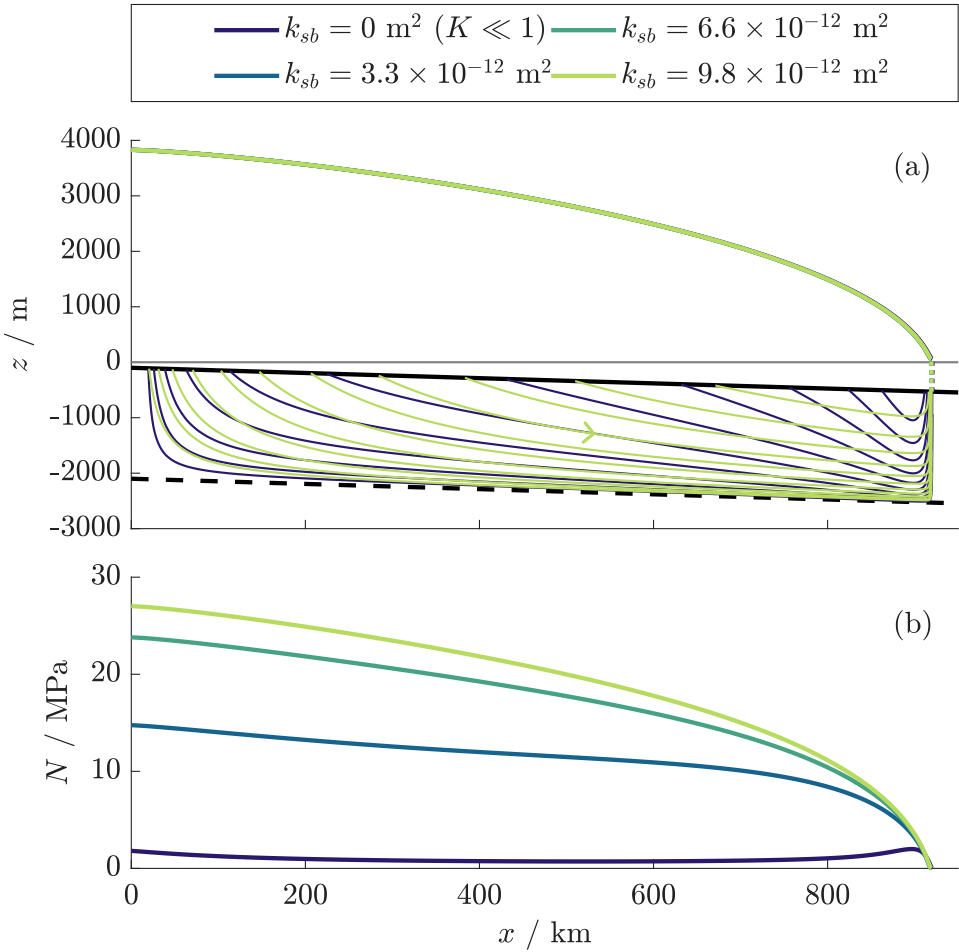


Figure 3: (a) Ice sheet profile and sedimentary basins, and (b) effective pressure for a relatively low melt rate $m = 10 \text{ mm yr}^{-1}$ (dimensionless $m = 1$), as in Figure 2(a), but with various values of k_{sb} corresponding to $K \ll 1$ and $K = 2, 4, 6$ respectively, and a uniform sedimentary basin depth $H_{sb} = 2000 \text{ m}$. The streamlines are only plotted for $k_{sb} = 0 \text{ m}^2$ and the maximum value of k_{sb} .

4 Steady ice sheet with strong groundwater flow

We now consider the steady states of the model when exfiltration and infiltration are strong enough to impact the hydrology and ice sheet, *i.e.* $K = O(1)$. As we have mentioned above, realistic values of K include both small values and $O(1)$ values up to around $K \approx 6$. We begin with the case of a uniform sedimentary basin thickness $H_{sb} = 2000 \text{ m}$ for simplicity, before considering the additional effect of variation in H_{sb} .

4.1 Low melt rate

We first consider the case where $m = 10 \text{ mm yr}^{-1}$ (dimensionless $m = 1$) is sufficiently small that the ice sheet is largely unaffected by subglacial hydrology, as seen in Figure 2(a). This enables us to observe the effect of groundwater on the effective pressure N with the ice sheet held roughly constant. Figure 3(a) shows the resulting ice sheet and streamlines, and Figure 3(b) shows the effective pressure.

The main outcome of including a sedimentary basin in this case is to increase the effective pressure N , with a greater increase for higher K . This can be seen from the $\mathcal{E} = 0$ approximate solution (30), and is a consequence of the fact that the total meltwater flux mx must be shared between the sedimentary basin and the cavity sheet, leading to a lower effective water thickness h . For the nonzero k_{sb} considered in this case, N attains unphysically large values.

The approximate solution (30) suggests for constant H_{sb} that the sedimentary basin has

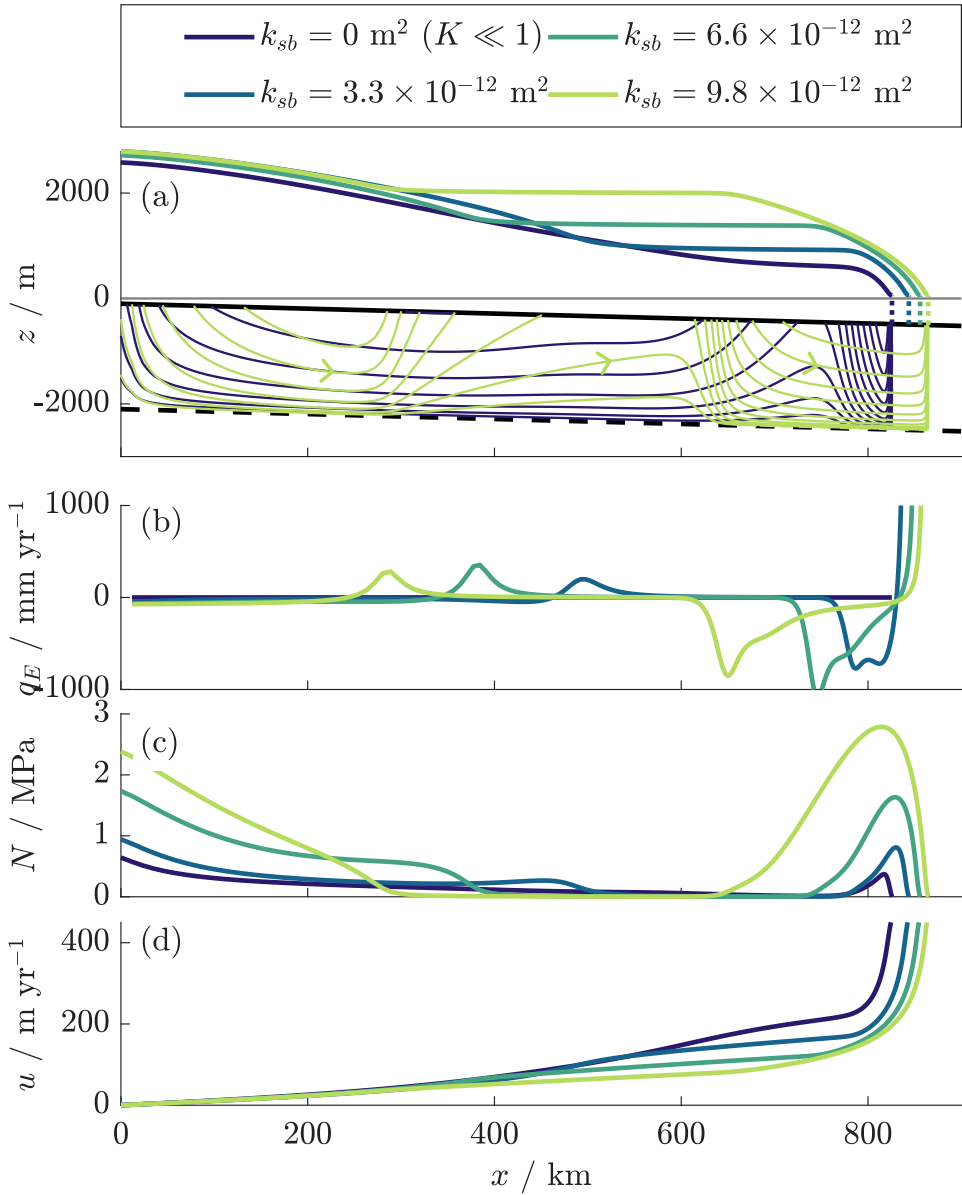


Figure 4: (a) Ice sheet profile and sedimentary basin streamlines, (b) exfiltration q_E , (c) effective pressure, and (d) ice velocity for a higher melt rate $m = 80 \text{ mm yr}^{-1}$ (dimensionless $m = 8$), as in Figure 2(b). The various values of k_{sb} , the sedimentary basin depth H_{sb} , and the plotted streamlines are as in Figure 3.

a larger effect when the distance from the ice divide x is small, or the hydraulic potential gradient is steep. When $m = 10 \text{ mm yr}^{-1}$, the hydraulic potential gradient becomes steeper with increasing x , so that these competing effects even out to a relatively uniform effect due to K . As predicted previously, N follows the $\psi = 0$ approximate solution (31) near the grounding line independent of K , so that the sedimentary basin has little effect on the extensional stress boundary layer of the ice and resulting grounding line position x_g .

4.2 High melt rate

Figure 4 shows the effect of strong groundwater flow on the steady state ice and hydrology for the higher melt rate $m = 80 \text{ mm yr}^{-1}$ (dimensionless $m = 8$), where the the hydrology affects the ice profile, as seen in Figure 2(b).

When the groundwater flow was weak, the low effective pressure resulted in a region of the ice with small surface slope, with a localised region of groundwater exfiltration slightly upstream. For strong groundwater flow, this exfiltration spreads the region of low effective

pressure further upstream, in turn causing the region of exfiltration to move upstream, as seen in Figure 4(b). The corresponding change in the effective pressure is seen in Figure 4(c). Away from this region of low effective pressure, the presence of a more permeable sedimentary basin increases N , with the effect strongest where the hydraulic gradient (*i.e.* the ice sheet profile) is steepest, near the ice divide and grounding line.

The effect on the ice sheet, along with the groundwater flow streamlines, is shown in Figure 4(a). As the region of low effective pressure moves upstream with increasing K , the corresponding region where the ice surface is relatively flat follows. The increase in effective pressure near the grounding line leads to a larger region where the basal friction is high, and the ice profile relatively steep as a result. This leads to a larger ice thickness overall, as ice accumulates behind the region of increased friction.

Since the ice flux is given by $Hu = ax$ in the steady state, the thickening of the ice sheet when K is increased results in a reduced ice velocity, as shown in 4(d).

Finally, we can observe a small advance of the grounding line as K is increased. This effect emerges because increasing K raises the effective pressure close to the grounding line at sub-leading order, similarly to if m were decreased.

These results indicate that groundwater flow in sedimentary basins has the potential to significantly affect on the steady-state thickness and velocity of an ice sheet. This is because the sedimentary basin can drain water away from certain regions of the subglacial hydrological system, locally increasing the effective pressure, and exfiltrate this water elsewhere to create regions of low effective pressure in a self-reinforcing feedback. The sedimentary basin also affects the steady grounding line position, albeit to a lesser extent. We infer that it is important to consider sedimentary basin groundwater flow in models for subglacial hydrology and basal friction, and that such groundwater flow could help to explain regions of locally high or low basal friction.

4.3 Effects of sedimentary basin geometry

So far we have worked with a uniform sedimentary basin thickness H_{sb} . However, previous work has found that shallowing and deepening of a sedimentary basin can drive exfiltration and infiltration respectively (Cairns et al., 2025). We therefore investigate the consequences of variations in sedimentary basin geometry in Figure 5, using an idealised sedimentary basin thickness $H_{sb} = 750 - 500 \cos(2\pi x/250 \text{ km})$ m. The ice sheet profile and streamlines for various K are shown in Figure 5(a), and we can see from the latter that several regions of exfiltration and infiltration emerge.

The effective pressure in Figure 5(b) shows the effect of this exfiltration and infiltration, which result in local peaks in N where the sedimentary basin is deepening (infiltration) and troughs where the sedimentary basin is shallowing (exfiltration). These are most prominent in the middle of the domain.

In the ice sheet in Figure 5(a), we can see the effect of these changes in the effective pressure on the ice profile. The local trough in effective pressure produces a plateau-like region of flatter surface slope, whereas the local peak produces a steeper region, resulting in a staggered shape. The net effect of this steepening and flattening on the ice thickness further inland is negligible, so that the effect of the sedimentary basin geometry is localised.

These results suggest, in addition to their permeability, the geometry of sedimentary basins is important in determining their effect on the ice sheet. Moreover, they suggest that the ice sheet profile may give an indication of the properties of the underlying sedimentary basin. In particular, regions of steeper or shallower ice may suggest a change in basal friction, which could be explained by local variations in sedimentary basin geometry driving exfiltration and infiltration.

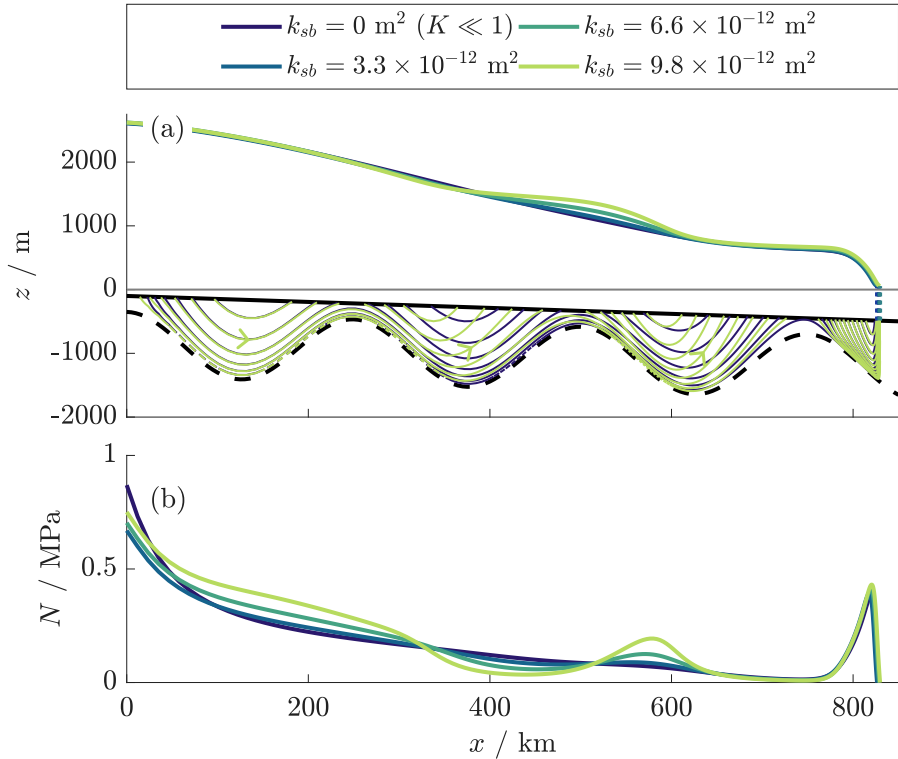


Figure 5: (a) Ice sheet profile and sedimentary basin streamlines and (b) effective pressure for a nonuniform sedimentary basin depth $H_{sb} = 750 - 500 \cos(2\pi x/250 \text{ km})$ m. The various values of k_{sb} and the plotted streamlines are as in Figures 3 and 4. (Note that in (a), as elsewhere, the aspect ratio is exaggerated for illustrative purposes.)

5 Groundwater feedback during grounding line motion

We now turn our consideration to transient solutions of the model, in order to investigate the effect of compaction-driven exfiltration. A canonical case is evolution of the system towards a steady state. This can be brought about when a parameter of the model, such as the Glen’s flow law parameter A , changes, meaning that the ice sheet is no longer in a steady state and must advance or retreat to a new one. This scenario has been investigated in prior studies of ice and hydrology (*e.g.* Lu and Kingslake, 2023)), and additionally resembles the behaviour of the ice after crossing ‘tipping points’ that can emerge from non-monotone bed geometry (Schoof, 2007a). A change in the temperature-sensitive A could represent, for example, a change in the climate.

In this section, we show that, when the ice is retreating towards a steady state, compaction-driven exfiltration provides a positive feedback that accelerates this retreat. Using the same linear prograde bed $b(x)$ as above, and with constant sedimentary basin thickness $H_{sb} = 2000$, melt rate $m = 10 \text{ mm yr}^{-1}$ and $k_{sb} = 1.6 \times 10^{-12} \text{ m}^2$, we initialise the system in a steady state with $A = 1 \times 10^{-25} \text{ s}^{-1} \text{ Pa}^{-3}$. We then step-change the value at time $t = 0$ to $A = 2 \times 10^{-25} \text{ s}^{-1} \text{ Pa}^{-3}$, so that the steady state is moved further back, requiring the ice sheet to retreat towards the new steady state. We repeat this scenario for different values of Σ , the parameter determining the strength of compaction-driven exfiltration, which are achieved by varying the parameter S_S . As mentioned previously, realistic values of S_S give Σ ranging from small to $O(1)$ values.

The results of this experiment are shown in Figure 6. Figure 6(a) compares the grounding line position $x_g(t)$ over time for various values of Σ . We can see that increasing Σ (via S_S) makes this retreat faster, with the effect beginning early on and persisting until the end of the experiment, at which the grounding line is significantly closer to the steady state for the maximum S_S than when $\Sigma = 0$. The mechanism behind this acceleration is shown in Figures

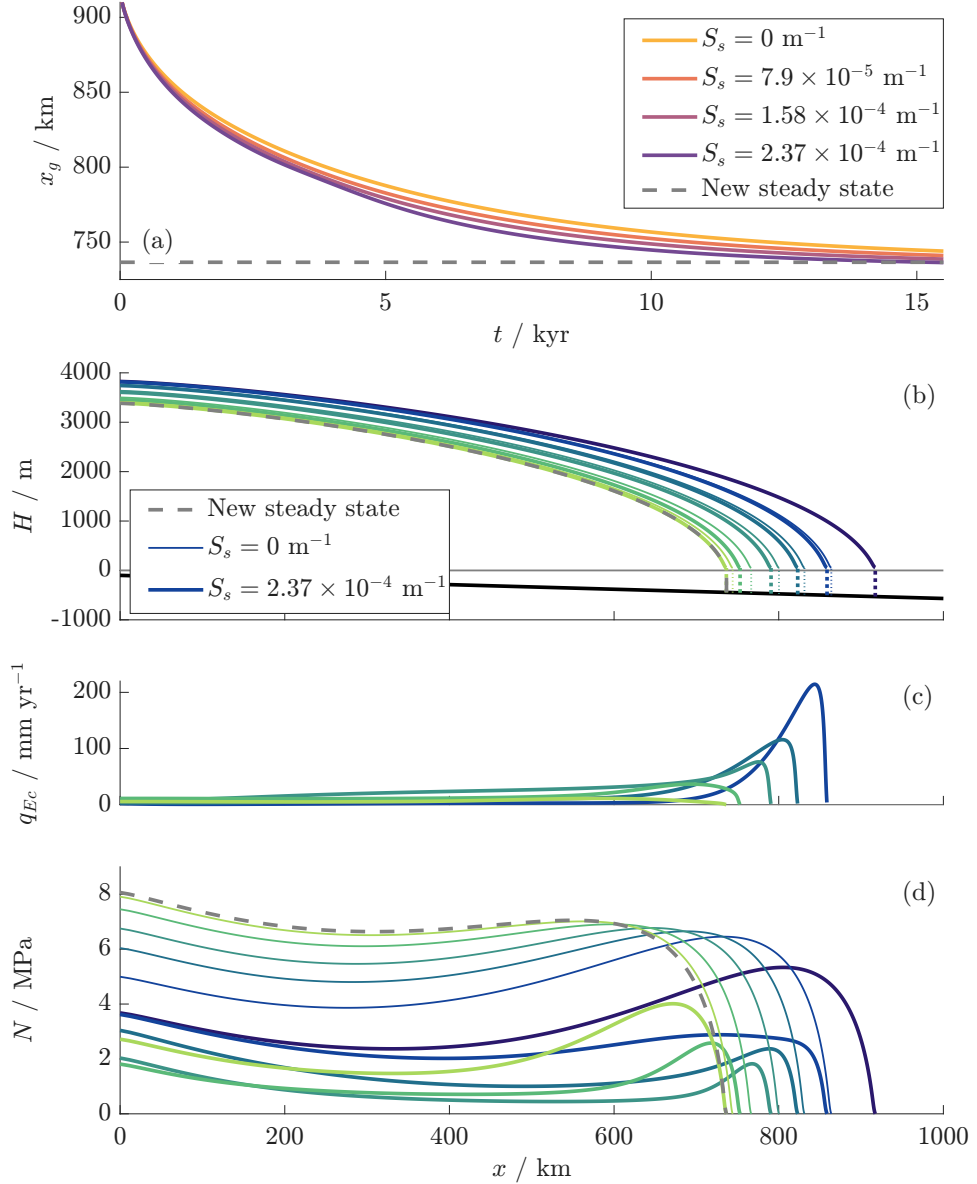


Figure 6: (a) Grounding line position $x_g(t)$, retreating to a steady state following a step increase in A , for various values of S_S corresponding to $\Sigma = 0, 4, 8, 12$ respectively, $m = 10 \text{ mm yr}^{-1}$, $k_{sb} = 1.6 \times 10^{-12} \text{ m}^2$, and otherwise as in Figure 3. (b) Ice sheet thickness H , (c) compaction-driven exfiltration q_{Ec} , and (d) effective pressure N , at times $t = 0, 0.8, 1.9, 3.9, 7.8, 15.4 \text{ kyr}$, for $S_S = 0$ and its maximum value above. A lighter and greener colour indicates later times.

6(b), (c) and (d), which show the ice sheet profile, the compaction-driven component of the exfiltration q_{Ec} (defined as the second term in Equation (21)), and the effective pressure N at selected points in time for the cases $S_S = 0 \text{ m}^{-1}$ and its maximum value ($\Sigma = 0$ and $\Sigma = 12$).

As seen in Figure 6(b), the retreat of the ice leads to ice thinning, which is most pronounced near the grounding line as the surface slope is steepest. When compaction-driven exfiltration is included, this thinning ($\partial H/\partial t < 0$) without an immediate corresponding change in N produces an exfiltration q_{Ec} , seen in Figure 6(c), which is strongest near the grounding line.

This exfiltration lowers the effective pressure, seen in Figure 6(c), by increasing the effective water thickness h . Although this lowering of N occurs across the domain, its effect on the ice sheet is largest near the grounding line. Here, the reduction in basal friction leads to faster sliding of the ice and hence a higher ice flux across the grounding line, resulting in a faster rate of grounding line retreat.

Rather than retreat, we can also consider grounding line advance following a step decrease in A . In this case, the ice thickens rather than thins, resulting in infiltration rather than exfiltration. This will increase the effective pressure and hence the basal friction, which results in slightly faster advance of the grounding line. However, the effect is weaker than its counterpart during retreat, because the grounding line moves away from where the effective pressure is most affected rather than towards it. Figure A1 (see Appendix) provides a counterpart to Figure 6 for the case of advance to confirm this behaviour.

A remaining question is how the strength of the response to compaction-driven exfiltration and infiltration varies with m and K . When $m = 0$, the effect is weak, because the effective pressure remains close to its steady state given identically by $\psi = 0$ throughout the retreat, so that very little exfiltration or infiltration occurs. However, for large m , the effect also weakens with increasing m , because the exfiltration contributes a relatively small change to the basal effective water thickness. It follows that the effect is maximised for an intermediate nonzero m . Due to the analogy between increasing K and decreasing m , it also follows that the response is strongest when K is not too large. A demonstration of this, by plotting the difference in grounding line position between the cases $S_S = 0 \text{ m}^{-1}$ and $S_S = 3.3 \times 10^{-5} \text{ m}^{-1}$ for a range of m and k_{sb} , is shown in Figure A2 (see Appendix).

The results of this section indicate that, as well as affecting the steady states, sedimentary basins can also influence the transient dynamics of ice-hydrology systems through the separate process of compaction-driven exfiltration and infiltration. The fact that compaction-driven exfiltration accelerates grounding line retreat more than advance has potential importance for the future of the Antarctic ice sheet, as it suggests that ice streams whose hydrology is affected by sedimentary basins may retreat more easily than they re-advance. For example, if a small change in forcing that leads to retreat is applied and then reversed, the feedback from sedimentary basins will increase the extent of the temporary retreat but will not have an equal effect on the re-advance.

6 Discussion

In this paper, we have developed an idealised two-way coupled model of ice flow and subglacial hydrology, including a sedimentary basin which exchanges groundwater with the basal hydrological system. We found that exfiltration generally occurs close to the grounding line and infiltration close to the ice divide, but that exfiltration can also occur inland where the ice profile is becoming flatter in the direction of flow. Exfiltration and infiltration can also be driven by shallowing and deepening of the sedimentary basin respectively.

Regions of exfiltration locally lower the effective pressure, and infiltration increases the effective pressure. If the sliding of the ice is dominated by the subglacial effective pressure, then this in turn leads to a steeper ice profile above areas of infiltration and a shallower plateau-like profile above areas of exfiltration. Overall, a deeper or more permeable sedimentary basin

leads to thicker and slower-flowing ice in the steady state, due to certain localised increases in effective pressure.

Transient changes in the basal water pressure also produce compaction-driven exfiltration when the water pressure decreases, and infiltration when it increases. During ice sheet retreat (for example due to a changing climate), such exfiltration accelerates the process of retreat by lowering the effective pressure, and consequently basal friction, near the grounding line. Conversely, infiltration during ice sheet advance accelerates this advance, but does so to a much lesser extent.

Our model includes a number of idealising assumptions, in order to be simple to use and easy to interpret. However, there are a number of ways in which the theory in this paper could be extended to represent other features of Antarctic groundwater flow.

Firstly, the model considers only one horizontal dimension, limiting its ability to be applied in modelling specific Antarctic ice streams. For instance, the equations of mass conservation are unable to capture tributary sources of ice or basal water, or lateral variations in sedimentary basin geometry. In particular, lateral narrowing or broadening of the sedimentary basin could drive groundwater exfiltration or infiltration respectively, similarly to vertical shallowing and deepening. Moreover, topographic variation could lead basal water to be routed in several different ways rather than simply flowing towards the grounding line as assumed in this model. Nonetheless, our definition of exfiltration and infiltration q_E in Equation (21) from sedimentary basins in this paper can easily be extended to two horizontal dimensions as

$$q_E = \nabla \cdot \left[\frac{k_{sb}}{\eta} H_{sb} \nabla (\rho_i g H - N + \rho_w g b) \right] - \frac{S_s(1-\xi)}{\rho_w g} H_{sb} \frac{\partial}{\partial t} (\rho_i g H - N), \quad (35)$$

and could therefore be coupled into existing state-of-the-art models for subglacial hydrology and ice flow.

Our model also assumes an isotropic and homogeneous permeability of the sedimentary basin, although this is unlikely to be accurate in reality. The assumption of isotropy is in fact unnecessary, since our model uses the Dupuit approximation, which treats vertical groundwater flow as instantaneous, so that only the horizontal permeability matters. The depth-integrated approach can also be extended to heterogeneous k_{sb} , by replacing k_{sb} with a depth average (Cairns et al., 2025). However, if the permeability is highly heterogeneous (*e.g.* due to the presence of faults, or large changes between rock strata), a Dupuit model may be altogether inappropriate, with a full two-dimensional model of groundwater flow required instead.

In this paper, we have only considered one choice of bed topography $b(x)$, given by a linear prograde bed. Previous studies have shown that more realistic bed topographies can lead to complex ice dynamics, such as multiple steady states, hysteresis, and ‘tipping points’ as a parameter such as A is varied (Schoof, 2007a). Although such cases are beyond the scope of this paper, our findings concerning the steady states and dynamic behaviour of this model generalise to more complex geometries. For instance, compaction-driven exfiltration and infiltration accelerate the grounding line retreat, or decelerate the grounding line advance, that occurs after a ‘tipping point’ emerging from bed topography is crossed.

We have also only considered a single sliding law, the regularised Coulomb law (4), in coupling the ice sheet to the hydrological system. A more comprehensive study could consider a range of sliding laws, along with different values of parameters such as \mathcal{C} and m_W (as in *e.g.* Brondex et al., 2019; Gregov et al., 2023)). However, the results of this study should generalise to any sliding law in which the basal stress is an increasing function of effective pressure, with the caveat that the parameters of the sliding law will determine the overall strength of the coupling.

Our treatment of subglacial hydrology, based on a simple cavity-sheet model, is also deliberately simplified in order to be easy to solve and understand. While a simple model of this form ought to broadly agree with more complex models over the long timescales we consider (De Fleurian, 2018), it overlooks many of the means by which basal water is transported, such

as subglacial channels. A model of this sort may therefore be inappropriate when considering shorter timescales (*e.g.* months to years), over which channels play an important role in Antarctic subglacial hydrology (Dow, 2022). Once again, this suggests that future work could focus on incorporating sedimentary basins into more detailed state-of-the-art models of subglacial hydrology, which are able to describe several modes of subglacial water transport.

The model in this paper could also be developed by including thermal effects. For example, rather than being treated as a constant parameter, the melt rate m could be calculated using an energy balance at the bed (as in *e.g.* Haseloff et al., 2025). This energy balance should include geothermal heating, along with basal friction and conduction from the ice. Such a model would allow for an investigation of how groundwater exfiltration from sedimentary basins could enhance the geothermal heat flux to the ice bed (Gooch et al., 2016), and the resulting impact on basal melting and subglacial hydrology. It would also enable the inclusion of basal freeze-on as an additional driver of exfiltration, as previously considered by Christoffersen and Tulaczyk (2003).

Overall, we have demonstrated how groundwater exchange with sedimentary basins may be incorporated into a model of subglacial hydrology coupled to ice sheet flow. Our research gives new insights into how such groundwater exchange could influence subglacial hydrology and, consequently, the dynamics of the ice sheet. This work highlights the need for further modelling, combined with observational data, in order to better understand the role of sedimentary basins in Antarctic subglacial hydrology, and the implications for Antarctica's contribution to future sea level rise.

Acknowledgments We thank Richard Katz and Dominic Vella for useful feedback on an early version of this manuscript.

Funding statement This research has been supported by UK Research and Innovation (grant no. EPSRC-2022).

Competing interests The authors declare none.

Data and code availability Code and data used to generate the figures in this paper may be found at <https://doi.org/10.5281/zenodo.18659557>.

Author contributions GJC, GPB, and IJH developed the model. GJC wrote the code and produced the results. GJC wrote the paper with input from GPB and IJH.

References

Aitken, A. R. A. e. a. (2023). Antarctic sedimentary basins and their influence on ice-sheet dynamics. *Reviews of Geophysics*, 61(3):e2021RG000767. e2021RG000767 2021RG000767.

Alley, R. B. (1996). Towards a hydrological model for computerized ice-sheet simulations. *Hydrological Processes*, 10(4):649–660.

Bear, J. (2013). *Dynamics of fluids in porous media*. Courier Corporation.

Brondex, J., Gillet-Chaulet, F., and Gagliardini, O. (2019). Sensitivity of centennial mass loss projections of the Amundsen basin to the friction law. *The Cryosphere*, 13(1):177–195.

Bueler, E. and Brown, J. (2009). Shallow shelf approximation as a “sliding law” in a thermomechanically coupled ice sheet model. *Journal of Geophysical Research: Earth Surface*, 114(F3).

Cairns, G., Benham, G., and Hewitt, I. (2025). Groundwater dynamics beneath a marine ice sheet. *The Cryosphere*, 19(9):3725–3747.

Christoffersen, P., Bougamont, M., Carter, S., Fricker, H., and Tulaczyk, S. (2014). Significant groundwater contribution to Antarctic ice streams hydrologic budget. *Geophysical Research Letters*, 41(6):2003–2010.

Christoffersen, P. and Tulaczyk, S. (2003). Thermodynamics of basal freeze-on: predicting basal and subglacial signatures of stopped ice streams and interstream ridges. *Annals of Glaciology*, 36:233–243.

Cook, S., Christoffersen, P., Todd, J., Slater, D., and Chauché, N. (2020). Coupled modelling of subglacial hydrology and calving-front melting at Store Glacier, West Greenland. *The Cryosphere*, 14(3):905–924.

Creyts, T. and Schoof, C. (2009). Drainage through subglacial water sheets. *Journal of Geophysical Research: Earth Surface*, 114(F4).

Cuffey, K. and Paterson, W. (2010). *The physics of glaciers*. Academic Press.

De Fleurian, B. e. a. (2018). SHMIP the subglacial hydrology model intercomparison project. *Journal of Glaciology*, 64(248):897–916.

Dow, C. (2022). The role of subglacial hydrology in Antarctic ice sheet dynamics and stability: a modelling perspective. *Annals of Glaciology*, 63(87-89):49–54.

Dow, C., Ross, N., Jeofry, H., Siu, K., and Siegert, M. (2022). Antarctic basal environment shaped by high-pressure flow through a subglacial river system. *Nature Geoscience*, 15(11):892–898.

Ehrenfeucht, S., Dow, C., McArthur, K., Morlighem, M., and McCormack, F. (2025). Antarctic wide subglacial hydrology modeling. *Geophysical Research Letters*, 52(1):e2024GL111386.

Engelhardt, H., Humphrey, N., Kamb, B., and Fahnestock, M. (1990). Physical conditions at the base of a fast moving Antarctic ice stream. *Science*, 248(4951):57–59.

Flowers, G. (2015). Modelling water flow under glaciers and ice sheets. *Proceedings of the Royal Society A: Mathematical, Physical and Engineering Sciences*, 471(2176):20140907.

Fowler, A. (1981). A theoretical treatment of the sliding of glaciers in the absense of cavitation. *Philosophical Transactions of the Royal Society of London. Series A, Mathematical and Physical Sciences*, 298(1445):637–681.

Fricker, H., Galton-Fenzi, B., Walker, C., Freer, B., Padman, L., and DeConto, R. (2025). Antarctica in 2025: Drivers of deep uncertainty in projected ice loss. *Science*, 387(6734):601–609.

Gagliardini, O., Cohen, D., Råback, P., and Zwinger, T. (2007). Finite-element modeling of subglacial cavities and related friction law. *Journal of Geophysical Research: Earth Surface*, 112(F2).

Gooch, B., Young, D., and Blankenship, D. (2016). Potential groundwater and heterogeneous heat source contributions to ice sheet dynamics in critical submarine basins of East Antarctica. *Geochemistry, Geophysics, Geosystems*, 17(2):395–409.

Gregov, T., Pattyn, F., and Arnst, M. (2023). Grounding-line flux conditions for marine ice-sheet systems under effective-pressure-dependent and hybrid friction laws. *Journal of Fluid Mechanics*, 975:A6.

Gustafson, C., Key, K., Siegfried, M., Winberry, J., Fricker, H., Venturelli, R., and Michaud, A. (2022). A dynamic saline groundwater system mapped beneath an Antarctic ice stream. *Science*, 376(6593):640–644.

Haseloff, M., Hewitt, I., and Katz, R. (2025). Subglacial hydrology regulates oscillations in marine ice streams. *EGUphere*, 2025:1–28.

Hayden, A.-M., Pelle, T., and Dow, C. (2025). The past, present, and future evolution of Aurora Subglacial Basin's subglacial drainage system. *Nature Communications*, 16(1):2747.

Helanow, C., Iverson, N., Woodard, J., and Zoet, L. (2021). A slip law for hard-bedded glaciers derived from observed bed topography. *Science Advances*, 7(20):eabe7798.

Joughin, I., Smith, B., and Schoof, C. (2019). Regularized Coulomb friction laws for ice sheet sliding: Application to Pine Island Glacier, Antarctica. *Geophysical research letters*, 46(9):4764–4771.

Kazmierczak, E., Gregov, T., Coulon, V., and Pattyn, F. (2024). A fast and unified subglacial hydrological model applied to Thwaites Glacier, Antarctica. *EGUphere*, 2024:1–36.

Le Brocq, A., Payne, A., Siegert, M., and Alley, R. (2009). A subglacial water-flow model for West Antarctica. *Journal of Glaciology*, 55(193):879–888.

Lemieux, J.-M. (2006). *Impact of the Wisconsinian glaciation on Canadian continental groundwater flow*. University of Waterloo Waterloo, Ont., Canada.

Lemieux, J.-M., Sudicky, E., Peltier, W., and Tarasov, L. (2008). Dynamics of groundwater recharge and seepage over the Canadian landscape during the Wisconsinian glaciation. *Journal of Geophysical Research: Earth Surface*, 113(F1).

Li, L. and Aitken, A. (2024). Crustal heterogeneity of Antarctica signals spatially variable radiogenic heat production. *Geophysical Research Letters*, 51(2):e2023GL106201. e2023GL106201 2023GL106201.

Li, L., Aitken, A., Lindsay, M., and Kulessa, B. (2022). Sedimentary basins reduce stability of antarctic ice streams through groundwater feedbacks. *Nature Geoscience*, 15(8):645–650.

Lu, G. and Kingslake, J. (2023). Coupling between ice flow and subglacial hydrology enhances marine ice-sheet retreat. *EGUsphere*, 2023:1–31.

MacAyeal, D. (1989). Large-scale ice flow over a viscous basal sediment: Theory and application to ice stream B, Antarctica. *Journal of Geophysical Research: Solid Earth*, 94(B4):4071–4087.

McCormack, F., Roberts, J., Dow, C., Stål, T., Halpin, J., Reading, A., and Siegert, M. (2022). Fine-scale geothermal heat flow in Antarctica can increase simulated subglacial melt estimates. *Geophysical Research Letters*, 49(15):e2022GL098539.

Morlighem, M., Seroussi, H., Larour, E., and Rignot, E. (2013). Inversion of basal friction in Antarctica using exact and incomplete adjoints of a higher-order model. *Journal of Geophysical Research: Earth Surface*, 118(3):1746–1753.

Muszynski, I. and Birchfield, G. (1987). A coupled marine ice-stream–ice-shelf model. *Journal of Glaciology*, 33(113):3–15.

Pelle, T., Greenbaum, J., Ehrenfeucht, S., Dow, C., and McCormack, F. (2024). Subglacial discharge accelerates dynamic retreat of Aurora subglacial basin outlet glaciers, East Antarctica, over the 21st century. *Journal of Geophysical Research: Earth Surface*, 129(7):e2023JF007513.

Robel, A., Sim, S., Meyer, C., Siegfried, M., and Gustafson, C. (2023). Contemporary ice sheet thinning drives subglacial groundwater exfiltration with potential feedbacks on glacier flow. *Science Advances*, 9(33):eadh3693.

Schoof, C. (2005). The effect of cavitation on glacier sliding. *Proceedings of the Royal Society A: Mathematical, Physical and Engineering Sciences*, 461(2055):609–627.

Schoof, C. (2007a). Ice sheet grounding line dynamics: Steady states, stability, and hysteresis. *Journal of Geophysical Research: Earth Surface*, 112(F3).

Schoof, C. (2007b). Marine ice-sheet dynamics. Part 1. The case of rapid sliding. *Journal of Fluid Mechanics*, 573:27–55.

Seroussi, H. e. a. (2024). Evolution of the Antarctic ice sheet over the next three centuries from an ISMIP6 model ensemble. *Earth's Future*, 12(9):e2024EF004561.

Sommers, A., Rajaram, H., and Morlighem, M. (2018). SHAKTI: Subglacial Hydrology and Kinetic, Transient Interactions v1.0. *Geoscientific Model Development*, 11(7):2955–2974.

Tankersley, M., Horgan, H., Siddoway, C., Caratori Tontini, F., and Tinto, K. (2022). Basement topography and sediment thickness beneath Antarctica's Ross ice shelf. *Geophysical Research Letters*, 49(10):e2021GL097371.

Tsai, V., Stewart, A., and Thompson, A. (2015). Marine ice-sheet profiles and stability under Coulomb basal conditions. *Journal of Glaciology*, 61(226):205–215.

Wearing, M., Dow, C., Goldberg, D., Gourmelen, N., Hogg, A., and Jakob, L. (2024). Characterizing subglacial hydrology within the Amery ice shelf catchment using numerical modeling and satellite altimetry. *Journal of Geophysical Research: Earth Surface*, 129(4):e2023JF007421. e2023JF007421 2023JF007421.

Weertman, J. (1957). On the sliding of glaciers. *Journal of Glaciology*, 3(21):33–38.

Werder, M., Hewitt, I., Schoof, C., and Flowers, G. (2013). Modeling channelized and distributed subglacial drainage in two dimensions. *Journal of Geophysical Research: Earth Surface*, 118(4):2140–2158.

Parameter	Value	Units	Source
$[x]$	5×10^5	m	
a	0.3	m yr^{-1}	Schoof (2007a)
g	9.8	m s^{-2}	
ρ_i	900	kg m^{-3}	
ρ_w	1000	kg m^{-3}	
C_W	7.6×10^6	$\text{Pa m}^{-\frac{1}{3}} \text{s}^{\frac{1}{3}}$	Schoof (2007a)
m_W	1/3		Schoof (2007a)
A	4.2×10^{-25}	$\text{s}^{-1} \text{Pa}^{-3}$	Schoof (2007a)
n	3		
C_C	0.47		
E	1×10^5	Pa m	
$[m]$	0.01	m yr^{-1}	Christoffersen et al. (2014)
k	4.0×10^{-8}	m^2	
η	10^{-3}	Pa s	
k_{sb}	1.6×10^{-12}	m^2	Cairns et al. (2025)
ξ	0.2		Robel et al. (2023)
S_s	3.3×10^{-5}	m^{-1}	Robel et al. (2023)

Table 1: Imposed parameters and scalings (given to 2 significant figures where applicable).

Parameter	Value	Units	Parameter	Value
$[H]$	2300	m	δ	0.1
$[t]$	7800	yr	ϵ	5.2×10^{-4}
$[u]$	64	m yr^{-1}	λ	1.2×10^{-3}
$[N]$	1.0×10^6	Pa	\mathcal{E}	0.05
$[h]$	0.097	m	\mathcal{C}	5
			K	1
			Σ	2

Table 2: Derived parameters and scalings (given to 2 significant figures where applicable).

Zhang, Y., Moore, J., Zhao, L., Werder, M., Gladstone, R., and Wolovick, M. (2024). The role of hydraulic conductivity in the Pine Island Glacier’s subglacial water distribution. *Science of The Total Environment*, 927:172144.

Zoet, L. and Iverson, N. (2020). A slip law for glaciers on deformable beds. *Science*, 368(6486):76–78.

A Non-dimensionalisation

In this section, we detail the procedure of non-dimensionalising the model presented in this paper. As we proceed, we will take certain scalings and parameters as imposed, and the values we choose are summarised in Table 1. We will use these in turn to derive further scales and parameters, whose values are shown in Table 2. We begin with the ice sheet model, which consists of Equations (1) and (2), combined with the sliding law (4), and with the boundary conditions (6), (7) and (8).

We assume as in Schoof (2007b), that scales $[x]$ and $[a]$ for the horizontal length of the ice sheet and the accumulation rate are provided, the former due to (e.g.) the size of the continental shelf or the regional extent of accumulation. We then obtain scales for the ice thickness $[H]$ and ice velocity $[u]$ by setting

$$[H][u] = [a][x], \quad C_W[u]^{m_W} = \rho_i g [H]^2 / [x]. \quad (36)$$

The first expression comes from the mass conservation equation (1), and the second from assuming a balance between the basal and driving stress in the momentum equation (2), with a Weertman or regularised Coulomb sliding law. The timescale is then given by

$$[t] = [x]/[u] = [H]/[a]. \quad (37)$$

We may rescale the variables in Equations (1) and (2) using these scales, and scaling b with $[H]$. We also assume we have a scale $[N]$ for the effective pressure, although we are presently yet to derive this. After this, we obtain the dimensionless equations

$$\frac{\partial H}{\partial t} + \frac{\partial}{\partial x}(Hu) = a, \quad (38)$$

$$4\varepsilon \frac{\partial}{\partial x} \left(H \left| \frac{\partial u}{\partial x} \right|^{1/n-1} \frac{\partial u}{\partial x} \right) - \mathcal{C}N \left(\frac{|u|}{|u| + (\mathcal{C}N)^{1/m_W}} \right)^{m_W} \text{sgn}(u) - H \frac{\partial}{\partial x}(H + b) = 0, \quad (39)$$

where the dimensionless parameters are given by

$$\varepsilon = \frac{A^{-1/n}([u]/[x])^{1/n}}{2\rho_i g[H]} \ll 1. \quad (40)$$

and

$$\mathcal{C} = \frac{C_C[N]}{C_W[u]^{m_W}}. \quad (41)$$

In addition, the boundary conditions (6), (43) and (8) become

$$u = 0 \quad \text{at} \quad x = 0. \quad (42)$$

$$H = -\frac{b}{1-\delta} \quad \text{at} \quad x = x_g. \quad (43)$$

$$4\varepsilon H \left| \frac{\partial u}{\partial x} \right|^{1/n-1} \frac{\partial u}{\partial x} = \frac{1}{2}\delta H^2 \quad \text{at} \quad x = x_g, \quad (44)$$

where

$$\delta = 1 - \frac{\rho_i}{\rho_w} \approx 0.1. \quad (45)$$

We next seek to non-dimensionalise the subglacial hydrology equation (9). In addition to the scales described above, we assume that a scale for subglacial water sources $[m]$ is provided, *e.g.* by considering the melt rate expected from estimated geothermal heat fluxes beneath Antarctica (McCormack et al., 2022). We scale q_E with $[m]$, working on the assumption that meltwater fluxes and exfiltration contribute similar amounts to subglacial water budgets (Christoffersen et al., 2014). We also assume that, away from the grounding line, the effective pressure is relatively small compared to the overpressure, an assumption consistent with the results of other subglacial hydrology modelling (*e.g.* Ehrenfeucht et al., 2025). This means that the size of the hydraulic potential ψ is dominated by the ice overpressure, which scales with $\rho_i g[H]$. Assuming that the source terms m and q_E are balanced by the flux divergence in Equation (9) (as is required for a steady state), we can then derive a scale for the subglacial water thickness h , and subsequently the effective pressure N via Equation (13)

$$[h] = \frac{\eta[x]^2[m]}{k\rho_i g[H]}, \quad [N] = \frac{E}{[h]}. \quad (46)$$

For a general $h(N)$, $[N]$ can be determined from this law using the given $[h]$. Under these scalings, the mass conservation equation (9) and closure relation (13) become

$$\lambda \frac{\partial h}{\partial t} = \frac{\partial}{\partial x} \left[h \frac{\partial}{\partial x} \left(H - \mathcal{E}N + \frac{b}{1-\delta} \right) \right] + m + q_E, \quad N = \frac{1}{h}, \quad (47)$$

where the dimensionless parameters are given by

$$\lambda = \frac{[h]}{[m][t]} = \frac{[a][h]}{[m][H]} \ll 1, \quad (48)$$

and

$$\mathcal{E} = \frac{[N]}{\rho_i g [H]}. \quad (49)$$

The boundary conditions (14) and (15) become:

$$h \frac{\partial}{\partial x} \left(H - \mathcal{E}N + \frac{b}{1-\delta} \right) = 0 \quad \text{at} \quad x = 0, \quad (50)$$

$$N = 0 \quad \text{at} \quad x = x_g. \quad (51)$$

The fact that λ is small (see Table 2) suggests that our assumption of a balance between the flux divergence and source terms in Equation (9) is appropriate.

In considering the exfiltration, we scale H_{sb} using the ice sheet thickness scale $[H]$, since sedimentary basins are typically hundreds to thousands of metres deep (Gustafson et al., 2022; Tankersley et al., 2022), and otherwise use the scalings provided in Tables 1 and 2. The dimensionless version of Equation (21) for q_E is then

$$q_E = K \frac{\partial}{\partial x} \left[H_{sb} \frac{\partial}{\partial x} \left(H - \mathcal{E}N + \frac{b}{1-\delta} \right) \right] - \Sigma H_{sb} \frac{\partial}{\partial t} (H - \mathcal{E}N), \quad (52)$$

where the dimensionless parameters are given by

$$K = \frac{k_{sb}[H]}{k[h]} = \frac{k_{sb}[H]^2 \rho_i g}{\eta[x]^2[m]}, \quad (53)$$

and

$$\Sigma = \frac{\rho_i S_s (1 - \xi) [H]^2}{\rho_w[m][t]}. \quad (54)$$

B Additional figures

In this section we include two additional figures, which support our discussion in Section 5 of the effect of compaction-driven exfiltration during grounding line motion. That section focused on the grounding line retreat following a step increase in the parameter A , whose results were shown in Figure 6.

Figure A1 is the counterpart of Figure 6 for the case where A instead undergoes a step decrease, leading to grounding line advance. We can confirm from Figure A1 our hypothesis that compaction-driven infiltration raises the effective pressure, and hence the basal friction, near the grounding line, and that the result is an acceleration of grounding line advance. However, this effect is weaker than the corresponding acceleration of grounding line retreat.

Figure A2 explores the effect of varying the parameters m and K (via k_{sb}) on this acceleration of grounding line retreat. This is achieved by plotting $\Delta x_g(t)$, the relative difference in the grounding line positions between the cases when $S_s = 0 \text{ m}^{-1}$ and $S_s = 3.3 \times 10^{-5} \text{ m}^{-1}$ ($\Sigma = 0$ and $\Sigma = 2$), over time for a range of m (Figure A2(a)) and k_{sb} (Figure A2(b)). A larger value of Δx_g implies a stronger enhancement of retreat. Figure A2(a) confirms that the effect vanishes for $m = 0 \text{ mm yr}^{-1}$, and that as m is increased the peak of Δx_g also increases, although the long-time value of Δx_g (*i.e.* the strongest overall acceleration) is maximised for a finite m . Figure A2(b) confirms that, since increasing K via k_{sb} has a similar effect to decreasing m , the peak of Δx_g is maximised when $K = 0$, but the strongest overall acceleration occurs for a finite value of K .

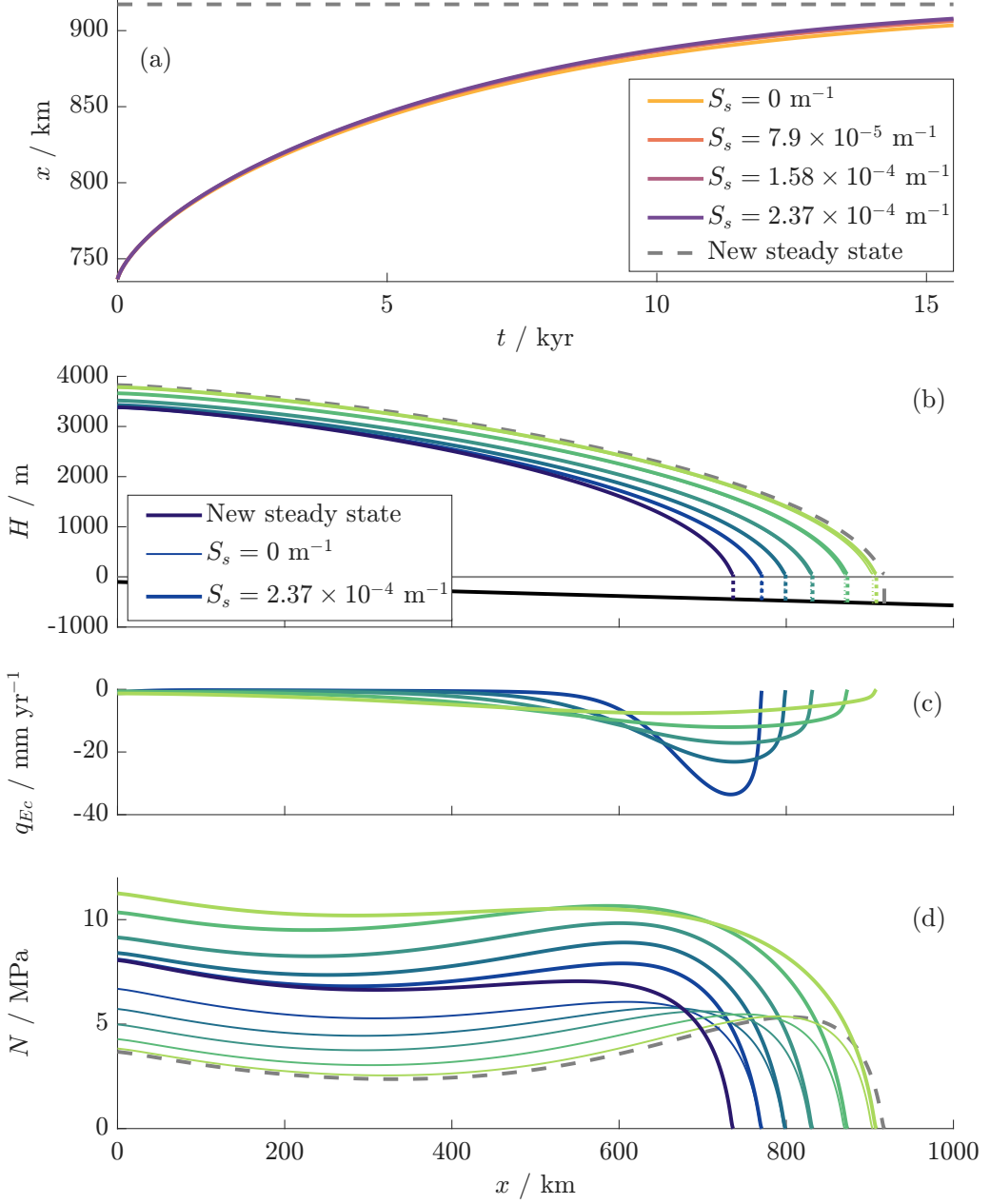


Figure A1: (a) Grounding line position $x_g(t)$, advancing to a steady state following a step decrease in A from $A = 2 \times 10^{-25} \text{ s}^{-1} \text{ Pa}^{-3}$ to $A = 1 \times 10^{-25} \text{ s}^{-1} \text{ Pa}^{-3}$, and otherwise as in Figure 6. (b) Ice sheet thickness H , (c) compaction-driven exfiltration q_{Ec} , and (d) effective pressure N , as in Figure 6.

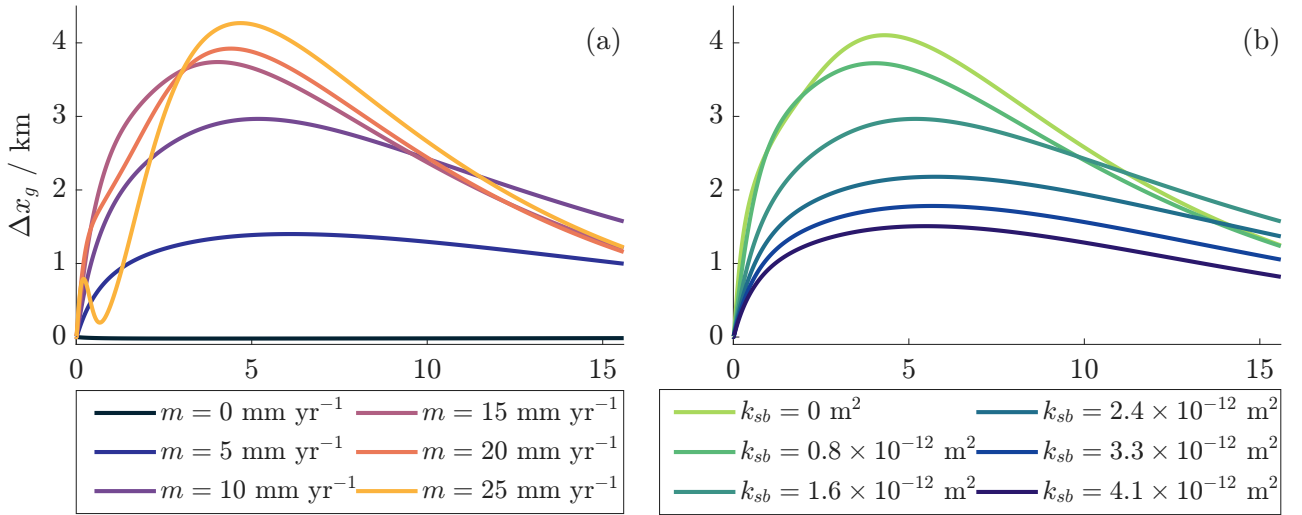


Figure A2: Difference in grounding line position $\Delta x_g(t)$ between the cases when $S_S = 0 \text{ m}^{-1}$ and $S_S = 3.3 \times 10^{-5} \text{ m}^{-1}$ ($\Sigma = 0$ and $\Sigma = 2$) for the retreat scenario considered in Figure 6, for (a) varying m corresponding to dimensionless $m = 0, 0.5, 1, 1.5, 2, 2.5$ with fixed $k_{sb} = 1.6 \times 10^{-12} \text{ m}^2$ (b) varying k_{sb} corresponding to $K = 0, 0.5, 1, 1.5, 2, 2.5$ with fixed $m = 10 \text{ mm yr}^{-1}$.